Synthesis and Characterization of Multilayered Supported Siliceous Shell and Metallic Core Nanocomposites: Catalyst for Decolorization of Methyl Violet Dye

Loganathan Bhojarajan [1,*] iD **, Gopalakrishnan Ravi** [2] **, Suresh Babu Nadarajan** [3] **, Chandraboss Vijayaragavan Lenin** [4] **, Krishnamoorthy Nanjundan** [5] **, Thangamani Kallapalayam Subramaniam** [1] **, Karthikeyan Balakrishnan** [6,*] iD

[1] Department of Chemistry (Science and Humanities), Dr. N.G.P. Institute of Technology, Coimbatore, Tamilnadu, India, 641048; br.loganathanvani@gmail.com (L.B.); thangamani@drngpit.ac.in (T.K.S.);

[2] Department of Physics (Science and Humanities), R.V.S. College of Engineering and Technology, Coimbatore, Tamilnadu, India, 641402; rgkrishnan12@gmail.com (G.R.);

[3] Department of Chemistry, Government College of Engineering-Sengipatti, Thanjavur, Tamilnadu, India, 613402; babusuresh1982@gmail.com (S.B.N.);

[4] Department of Chemistry, Malla Reddy Engineering College for Womens (MRECW), Maisammaguda, Secunderabad, Telangana, India, 500100; chandraboss08@gmail.com (C.V.L.);

[5] Department of Physics, Sri Eshwar College of Engineering, Coimbatore, Tamilnadu, India, 641202; yenkrish.spectrum@gmail.com (K.N.);

[6] Department of Chemistry, Annamalai University, Chidambaram, Tamilnadu, India, 608002; bkarthi_au@yahoo.com (K.B.);

* Correspondence: bkarthi_au@yahoo.com (K.B.); br.loganathanvani@gmail.com (L.B.);

Abstract: Herein, we have reported the synthesis and characterization of multilayered supported siliceous shell and metallic core nanocomposites (Au/Pt/Rh@SiO$_2$ nanocomposites) through the sol-gel chemical route. The developed methodology was rapid, facile, and eco-friendly. The physicochemical characterization was performed by atomic force microscopy (AFM), high-resolution transmission electron microscopy (HR-TEM), field emission scanning electron microscopy (FE-SEM), nitrogen adsorption-desorption, and UV-Visible diffuse reflectance spectroscopy (UV-Vis-DRS) methods. Texture properties of the catalyst particles are also calculated by applying the Brunauer-Emmett-Teller (BET) equation to the sorption isotherms. The as-synthesized nanocatalyst exhibited high catalytic decolorization of organic dyes, such as methyl violet (MV), with a decolorization efficiency of ~100 % in a short interval. The photocatalytic decolorization of MV was measured spectrophotometrically at their respective λmax values.

Keywords: multilayer supported siliceous shell; metallic core nanocomposites; decolorization.

1. Introduction

Since Pt-based nanocomposites comprising more than one metal exhibit multifarious structural features, they are an indispensable choice in selecting heterogeneous catalysts for an array of applications [1-4]. In the development of nanomaterials, functional materials act as a driving force due to their unique properties [5]. Among the various functional materials developed, the fabrication of core-shell nanocomposites has significantly attracted and acclaimed considerable attention [5-18]. Among the core-shell composites, metallic cores with

siliceous shells, in which the core (inner part) is composed of multimetallic nanoparticles and the shell (outer part) is compiled with silica spheres, are studied with a special interest due to their biocompatibility [10,19]. These nanocomposites find applications in catalysis, fuel cell, and drug delivery systems.

Most organic pollutants can be degraded by photocatalysis under UV & visible light irradiation [20-25]. Photocatalysts such as Au/Pt/Rh@SiO$_2$ nanocomposites possess the advantages of high stability and biological inertness. Therefore, photocatalytic decolorization of methyl violet in an aqueous solution is widely employed to deal with wastewater.

This paper presents a study on the decolorization of MV in an aqueous solution by multilayered supported siliceous shell and metallic core nanocomposites (Au/Pt/Rh@SiO$_2$ nanocomposites) through a sol-gel chemical route. Structural, morphological, and textural properties characterized the composite. The synergistic effect and surface adsorption of the MV dye on the Au/Pt/Rh@SiO$_2$ nanocomposite was systematically evaluated. In addition, the effect of dye concentration, catalyst dosage, and stability of the photocatalyst on the decolorization was examined. Absorbance analysis confirmed the decolorization of MV, and a mechanism has been proposed based on experimental and theoretical calculations.

2. Materials and Methods
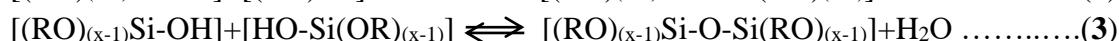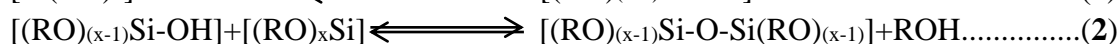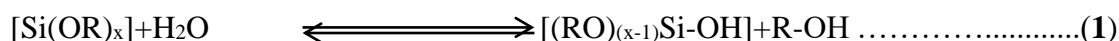
2.1. Chemicals and materials.

The salts, such as HAuCl$_4$.3H$_2$O (99.99%), H$_2$PtCl$_6$.xH$_2$O (98%), and RhCl$_3$.3H$_2$O (98%), were purchased from Hi-Media Laboratories. 3-Aminopropyl triethoxy silane (APTES), trisodium citrate (99.5%), tetraethoxysilane (TEOS), methyl violet (MV), and distilled ethanol was purchased from Nice Chemicals. Conductivity water with a resistivity of around 18.0 MΩ cm was used wherever required.

2.2. Synthesis of trimetallic Au/Pt/Rh colloidal nanocomposite doped amine-functionalized silica nanocomposite (Au/Pt/Rh@SiO$_2$ nanocomposite).

Au/Pt/Rh@SiO$_2$ nanocomposite was synthesized using the sol-gel method. In a typical protocol, 10 mL of APTES and 30 mL of TEOS were dissolved in 60 mL ethanol and stirred for 120 min. To this, 6 mL of pre-synthesized Au/Pt/Rh trimetallic colloidal nanocomposite (TNC) (The preparation procedure can be accessed from the Supplementary Information) was introduced, and stirring was continued further for 120 min, whereby the sol-gel mixture was obtained. Then, it was allowed to age and dry in an air oven at 100 °C for 24 h. Au/Pt/Rh@SiO$_2$ nanocomposite was obtained finally by grinding the zero-gel matrix.

2.3. Sol-gel process.

In the sol-gel process, a homogeneous aqueous ethanol solution of TEOS and Si(OR)$_x$ is obtained [26-28] initially, during which the R-O bond is hydrolyzed to form the Si-OH bond (Eqn. 1). Subsequently, the products condense in either of the two ways as given by Equations 2 and 3 resulted in the formation of Si-O-Si networks.

$$[Si(OR)_x] + H_2O \rightleftharpoons [(RO)_{(x-1)}Si\text{-}OH] + R\text{-}OH \dots\dots\dots\dots\dots (1)$$

$$[(RO)_{(x-1)}Si\text{-}OH] + [(RO)_x Si] \rightleftharpoons [(RO)_{(x-1)}Si\text{-}O\text{-}Si(RO)_{(x-1)}] + ROH \dots\dots\dots (2)$$

$$[(RO)_{(x-1)}Si\text{-}OH] + [HO\text{-}Si(OR)_{(x-1)}] \rightleftharpoons [(RO)_{(x-1)}Si\text{-}O\text{-}Si(RO)_{(x-1)}] + H_2O \dots\dots\dots (3)$$

In addition to this, APTES was added for the synthesis of amine-functionalized silica nanocomposites. Therefore, the expected product is shown below in Equation 4.

Amine functionalized $[(RO)_{(x-1)}Si\text{-}O\text{-}Si(RO)_{(x-1)}]$……………………………(**4**)
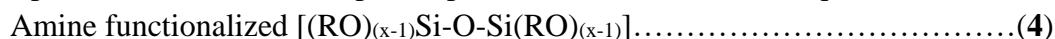
2.4. Photocatalysis experiment.

For the light-induced catalytic activity assessment of the catalysts in the decolorization of MV (0.2×10^{-4} M, 45 mL) at room temperature, a mercury vapor lamp (8 W, $\lambda_{max} = 365$ nm) was employed. The reaction mixture was stirred in the dark for 30 minutes, and the catalytic reactions were monitored spectrophotometrically (Shimadzu UV-1650 PC spectrophotometer) using 4 mL of the samples drawn periodically and centrifuged. Using the following formula, the decolorization of MV was calculated.

Decolorization $(\%) = (A_o - A / A_o) \times 100$ ……..………………………………...(**5**)

where A_o and A refer to the absorbance intensity of MV dye before and after the irradiation reaction, respectively.

2.5. Structural analysis.

A UV-vis (ultraviolet and visible light) spectrophotometer (Shimadzu, UV-1650 PC) was used to record the absorbance spectra of the samples at room temperature.

Surface topography of SiO_2 and Au/Pt/Rh@SiO_2 nanocomposites were analyzed using an AGILENT-N9410A series 5500 AFM instrument (Si cantilever; curvature radius = 10 nm) in tapping mode.

The surface characteristics of the samples were studied in detail using a JEOL 3010 HRTEM microscope with an ultra-high resolution polepiece operating at an accelerating voltage of 300 kV and a field-emission electron microscope (SUPRA 55-CARL ZEISS, Germany) operating at 20 kV.

The N_2 adsorption-desorption isotherms were obtained on a Micromeritics ASAP 2020 V3. 00 H instrument at -196 °C. The specific surface areas of the samples were determined by the Brunauer-Emmett-Teller (BET) method.

The UV-visible diffuse reflectance spectra were obtained on a UV-3600 SHIMADZU (Japan) spectrometer in the range 800-200 nm.

2.6. Computer simulations.

All calculations were carried out using Gaussian 03 [29]. For the optimization of the ground state geometries of SiO_2 and $Si_9O_{18}Rh_6$, the Density functional theoretical (DFT) with B3LYP functional [30, 31] was used, and the basis set used Lanl2DZ [32].

3. Results and Discussion

3.1. Atomic Force Microscopy (AFM) analysis.

The 2-dimensional and 3-dimensional AFM images of the undoped SiO_2 film displayed in Figure 1(a and b) show an even rough surface without any characteristic variations. The particle distribution curve depicted in Figure 1(c) shows the particle size to be 23 nm. However, the size is reduced to 6-9 nm (Figure 2(a)) when doped with Au/Pt/Rh TNCs, suggesting a particle-like character. The 3-dimensional AFM image (Figure 2(b)) reveals the presence of metal nanoparticles in Au/Pt/Rh@SiO_2. Thus, a structural variation between the

undoped SiO_2 and the $Au/Pt/Rh@SiO_2$ nanocomposites has been established. The trimetallic nanocomposite has a rough surface with a particle size of 8 nm, as confirmed by the particle distribution curve (Figure 2(c)).
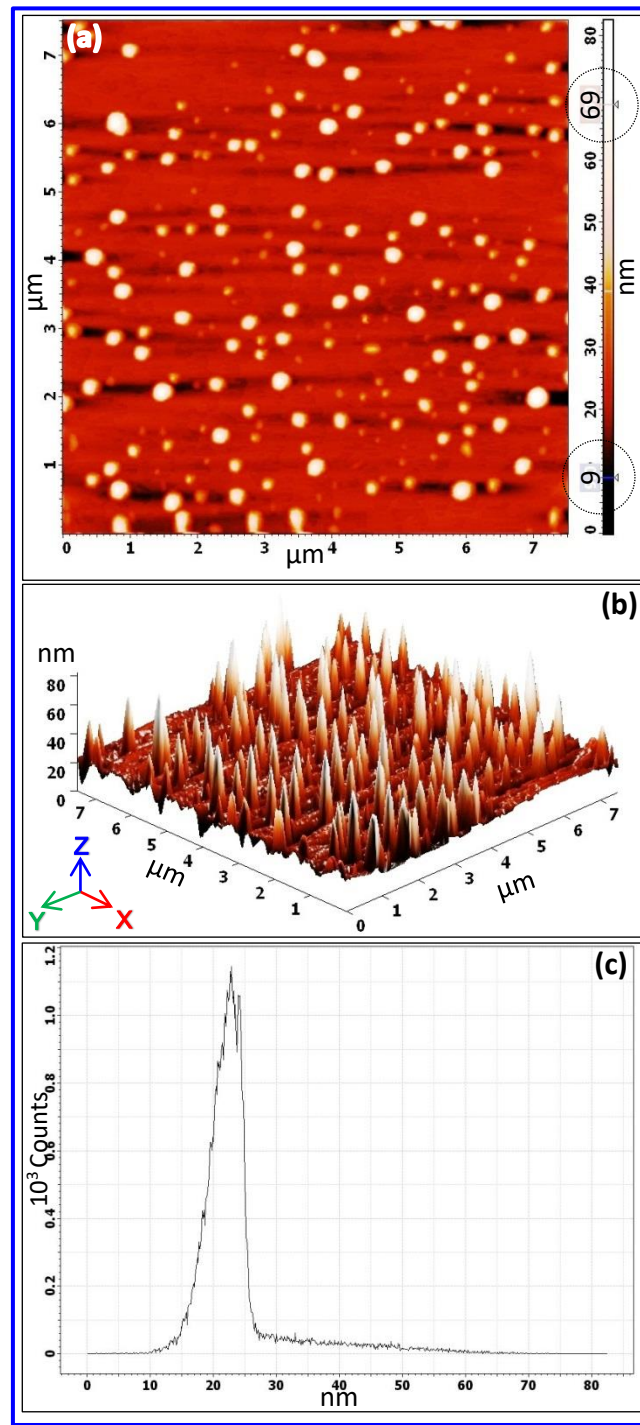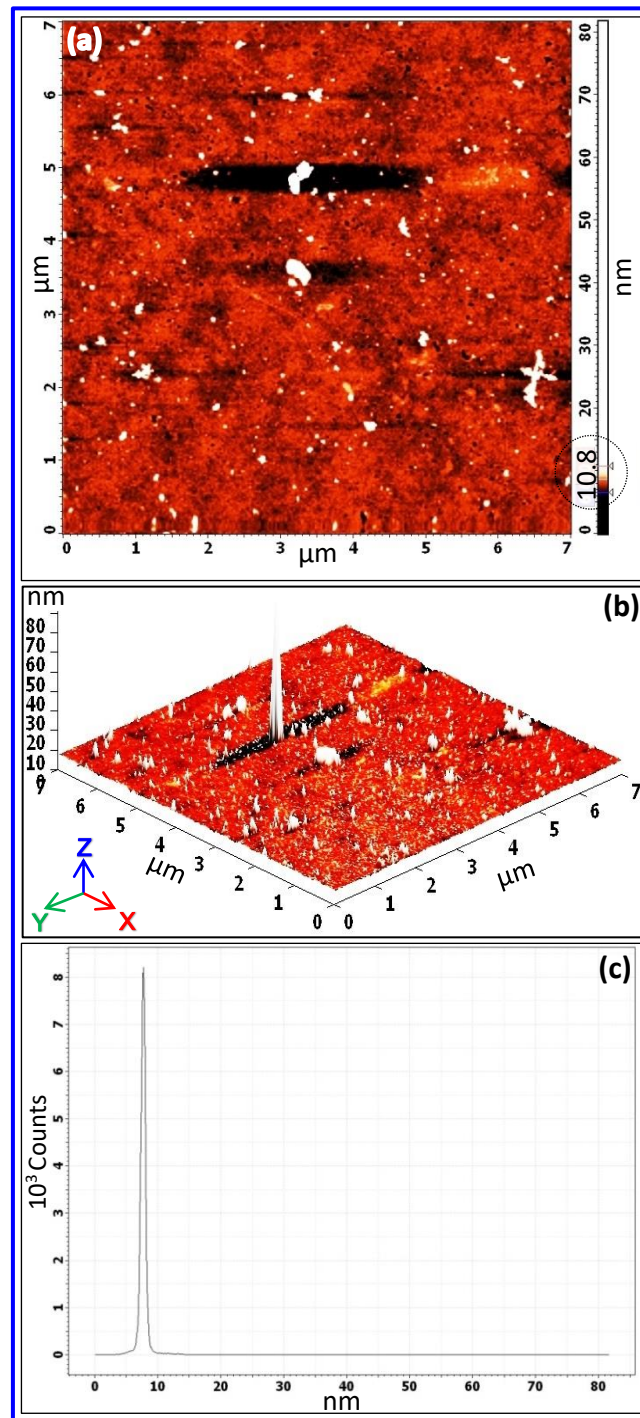

Figure 1. (**a**) Two-dimensional (2D) Atomic force microscopy (AFM) image (*height scale,* 80 nm; *scan size,* 7 μm X 7 μm), (**b**) Three-dimensional (3D) AFM image (7 μm by 7 μm), (**c**) AFM histogram of SiO_2 nanocomposite.

Figure 2. (**a**) Two-dimensional (2D) Atomic force microscopy (AFM) image (***height scale,*** 80 nm; ***scan size,*** 7 μm X 7 μm), (**b**) Three-dimensional (3D) AFM image (7 μm by 7 μm), (**c**) AFM histogram of Au/Pt/Rh@SiO$_2$ nanocomposite.

3.2. High-resolution Transmission electron microscopy (HR-TEM) analysis.

The HR-TEM images of Au/Pt/Rh@SiO$_2$ nanocomposites (Figure 3) confirm the structural morphology. Line plot profiles of the selected particles are highlighted in Figure 3(a and b). The nanoparticles are spherical, in which an electron-dense core (dark colored) is enclosed by an electron-thin shell (light-colored) form (Figure 3(c-f)). The 3D surface plot (Figure 3(d)) validates the core form of the nanocomposite. Figure 3(h and i) also suggested the formation of core@shell form. The selected area electron diffraction (SAED) pattern of Au/Pt/Rh@SiO$_2$ nanocomposites (Figure 3(j) attests to the amorphous nature of the nanocomposite.
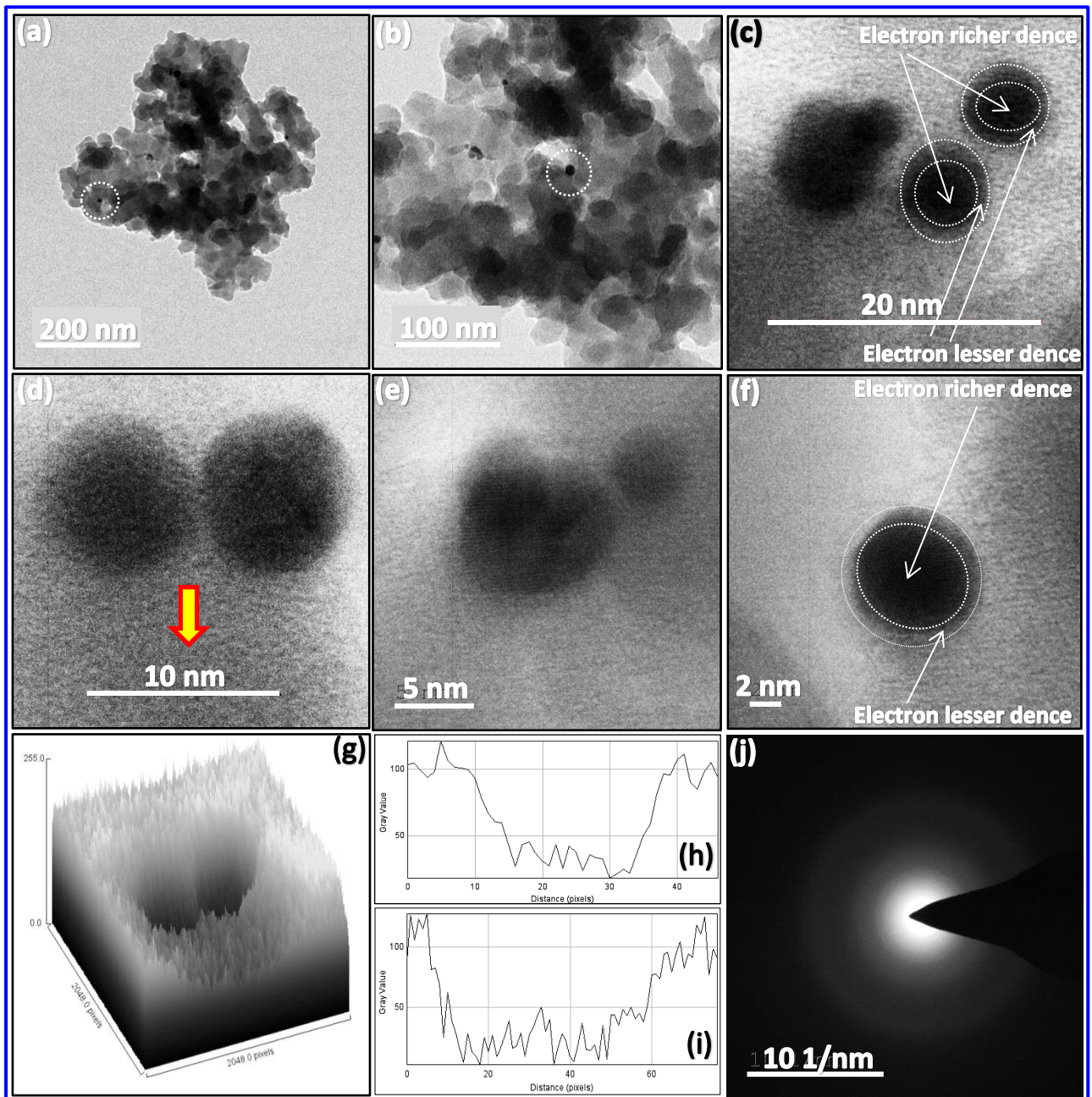
Figure 3. (a-f) High-resolution transmission electron microscopy (HR-TEM) images of Au/Pt/Rh@SiO$_2$ nanocomposite, *scale bars* (**a**) 200, (**b**) 100, (**c**) 20, (**d**) 10, (**e**) 5 and (**f**) 2 nm respectively (**g**) surface plot of the image (selected image is in (**d**)), (**h** and **i**) plot profile of the selected particles highlighted in (**a** and **b**) respectively and (**j**) selected area electron diffraction (SAED) pattern of Au/Pt/Rh@SiO$_2$ nanocomposite.

3.3. Field-emission scanning electron microscopy (FE-SEM) and Energy-dispersive X-ray (EDX) spectroscopy analysis.

The FE-SEM images of SiO$_2$ and Au/Pt/Rh@SiO$_2$ nanocomposites with different magnifications (Figure 4) clearly show their spherical morphology. "Image J viewer" was used to confirm the shell formation, and the line plot profile was also evaluated (inset of Figure 4(d)). Figures 4e and 4f approve of the formation of a shell of even electron density.
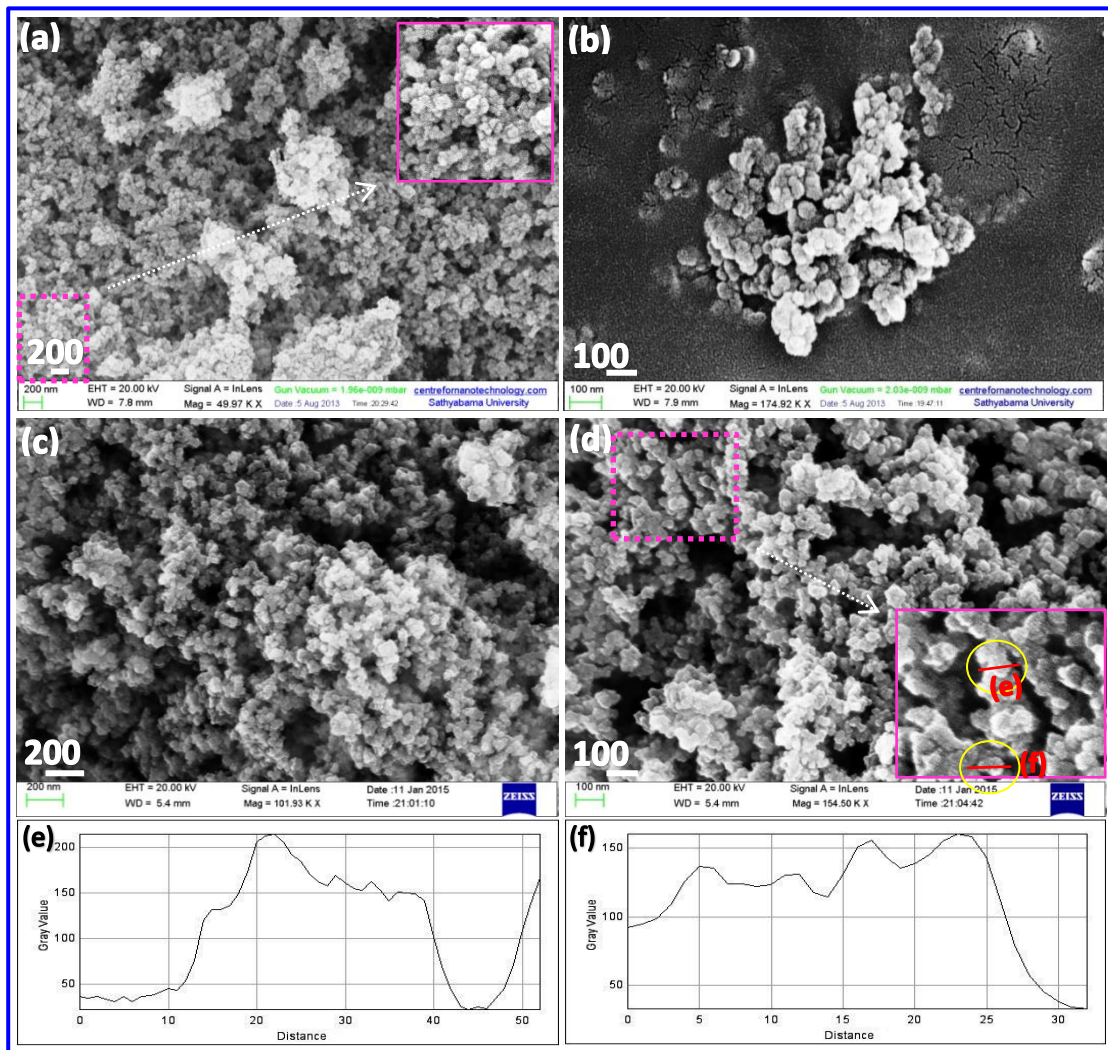
Figure 4(a and **b).** Field-emission scanning electron microscopy (FE-SEM) images of the SiO$_2$ nanocomposite with different magnifications, *magnification*: (**a**) 49.97K and (**b**) 174.92K, *scale bars*: (**a**) 200 and (**b**) 100 nm and (**c** and **d**). FE-SEM images of the Au/Pt/Rh@SiO$_2$ nanocomposite with different magnifications, *magnification*: (**c**) 101.93K and (**d**) 154.50K, *scale bars*: (**c**) 200 and (**d**) 100 nm, (**e**) and (**f**) line plot profile of the selected image (highlighted in (**d**)).

The results of elemental analysis of SiO$_2$ and Au/Pt/Rh@SiO$_2$ nanocomposites by EDX are presented in Figure 5(a) and (b), respectively. The images show the presence of Si in SiO$_2$ and Si, Au, Pt, and Rh in the nanocomposite.
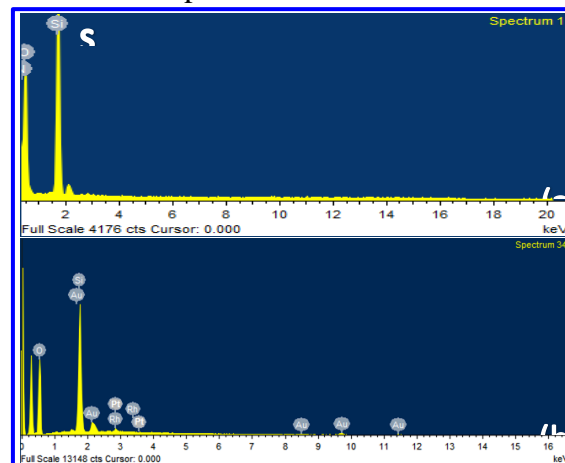

Figure 5. Elemental analysis by energy dispersive X-ray (EDX) spectroscopy of (**a**) SiO$_2$ and (**b**) Au/Pt/Ag@SiO$_2$ nanocomposite.

3.4. Textural properties.

The N_2 sorption isotherms, Brunauer-Emmett-Teller (BET) surface area plot, and Barrett-Joyner-Halenda (BJH) desorption pore distribution curve of the Au/Pt/Rh@SiO$_2$ nanocomposite is given in Figure 6 (a-c) (note: corresponding N_2 sorption isotherms, BJH desorption pore distribution and BET surface area plot of bare SiO$_2$ are given in Figure S1). The isotherms show (Figure 6(a)) type-III behavior. Furthermore, the H3-type hysteresis curve authenticates the mesoporous structure [10, 33-35]. The observation of an increasing step within the adsorption branch, along with a sharp decline in the desorption branch (Figure 6(a)), strongly confirms the mesoporosity [10, 36].
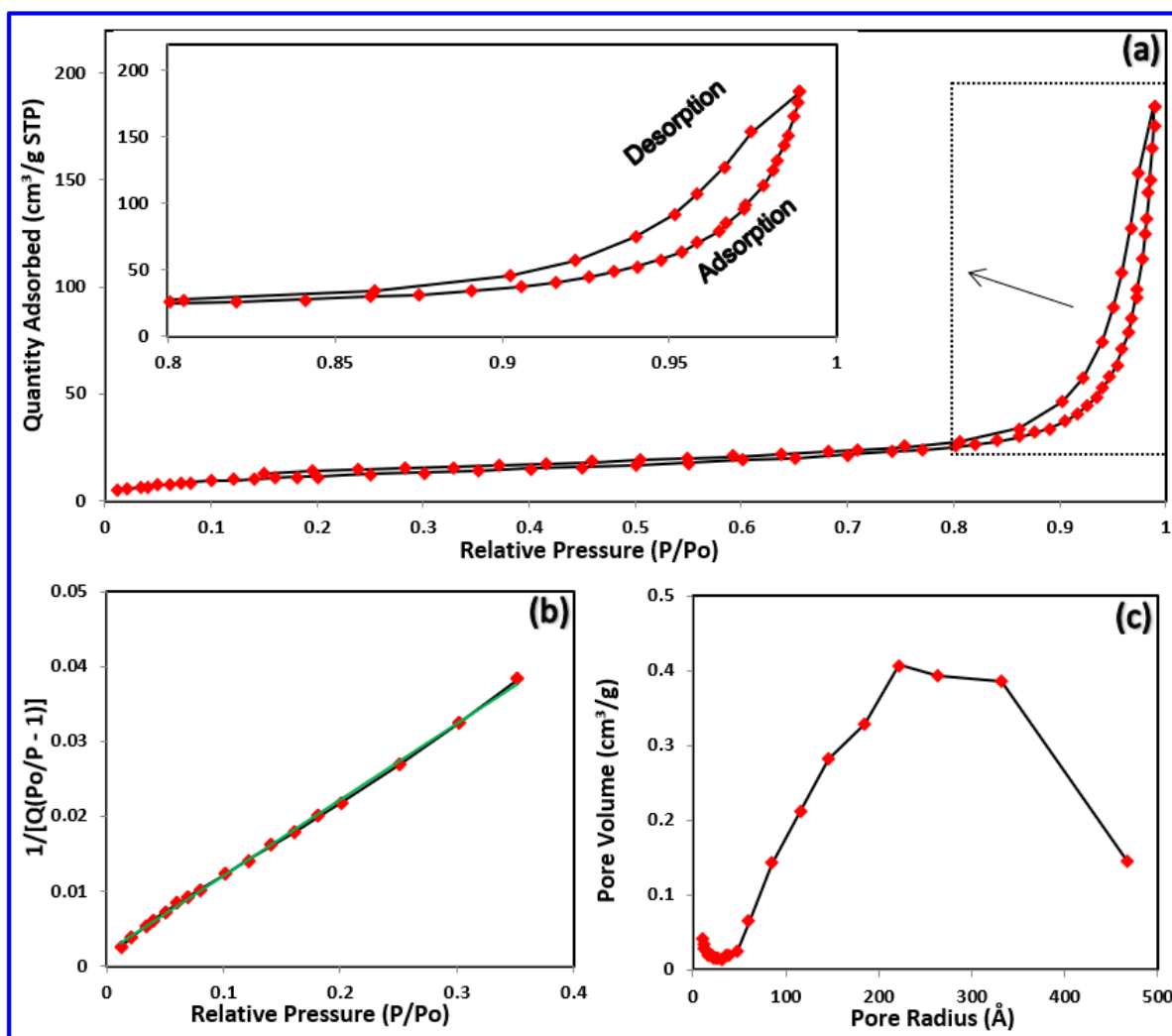

Figure 6. (**a**) Isotherm linear plot (nitrogen adsorption-desorption isotherms),
(**b**) Brunauer-Emmett-Teller (BET) surface area plot,
(**c**) Barrett-Joyner-Halenda (BJH) desorption pore volume of Au/Pt/Rh@SiO$_2$ nanocomposite.

Table 1. Structural parameters of the SiO$_2$ and Au/Pt/Rh@SiO$_2$ photocatalysts under UV-A light irradiation

Photocatalyst	BJH desorption average pore radius (Å)	V_T (cm^3/g)	S_{BET} (m^2/g)
SiO$_2$ nanopowder	123	0.28	40
Au/Pt/Rh@SiO$_2$ nanopowder	125	0.30	42

V_T is the total pore volume at relative pressure 0.98;

S_{BET} is the specific surface area deducted from the isotherm analysis in the relative pressure range from 0.0-1.0.

The relevant parameters are collected in Table 1. All parameters were higher for Au/Pt/Rh@SiO$_2$ nanocomposite compared to bare SiO$_2$ nanoparticles, suggesting better photocatalytic activity of Au/Pt/Rh@SiO$_2$ nanocomposite.

3.5. UV-Vis-diffuse reflectance spectral (UV–Vis-DRS) analysis.

Figure 7 shows the diffuse reflectance spectra of the undoped and doped SiO$_2$ nanocomposites. The pure SiO$_2$ exhibits only a feeble response supported by a band edge. On the other hand, doping enhanced light absorption due to the possible charge transfer transition. The reflectance spectra of the two samples in terms of recorded diffuse reflection employing the Kubelka-Munk algorithm are shown in Figure 8.
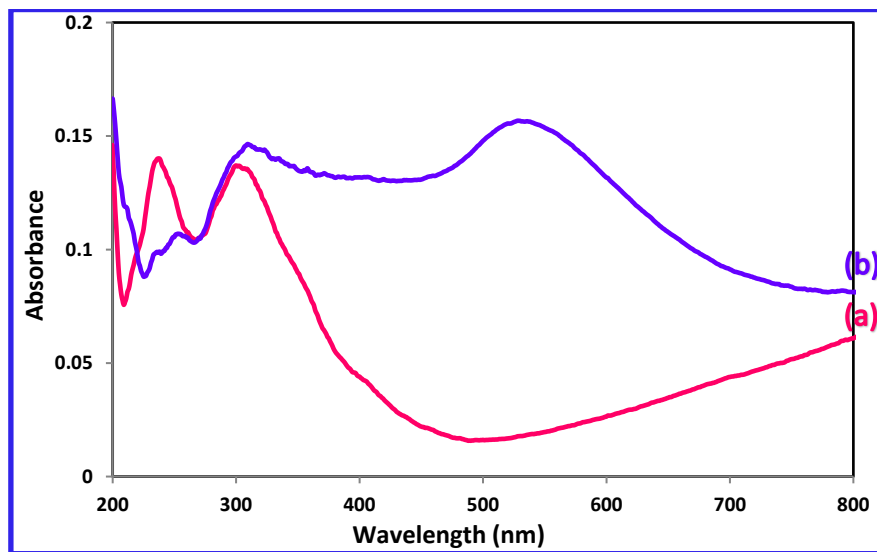

Figure 7. UV-vis-Diffuse reflectance spectrum (UV-vis-DRS) of (**a**) SiO$_2$ and (**b**) Au/Pt/Rh@SiO$_2$ nanocomposite (recorded with absorbance mode).
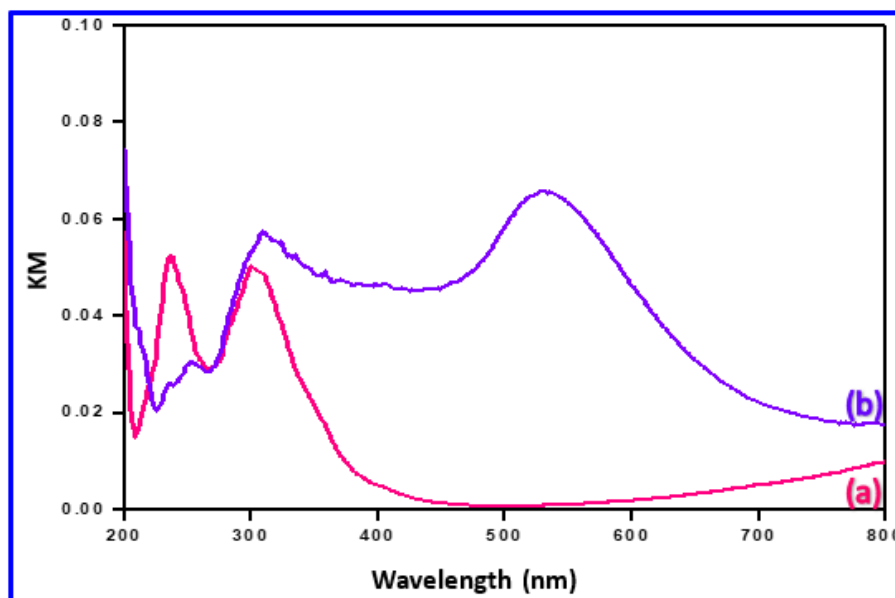

Figure 8. Diffuse reflectance spectra of (**a**) SiO$_2$ and (**b**) Au/Pt/Rh@SiO$_2$ nanocomposite.

Figure 9 depicts the band gaps of the samples obtained from the Tauc plots. Plots of (a) $[F(R)h\upsilon]^2$ vs. ($h\upsilon$) and (b) $[F(R)h\upsilon]^{0.5}$ vs. $h\upsilon$ provide the direct and indirect band gap energy. The direct and indirect band gaps of SiO$_2$ were found to be 5.51 and 5.22 eV, while those of Au/Pt/Rh@SiO$_2$ nanocomposites were 5.46 and 5.13 eV, respectively. The decrease in the

values of the Au/Pt/Rh@SiO$_2$ nanocomposite compared with the undoped SiO$_2$ should account for the superior catalytic activity.
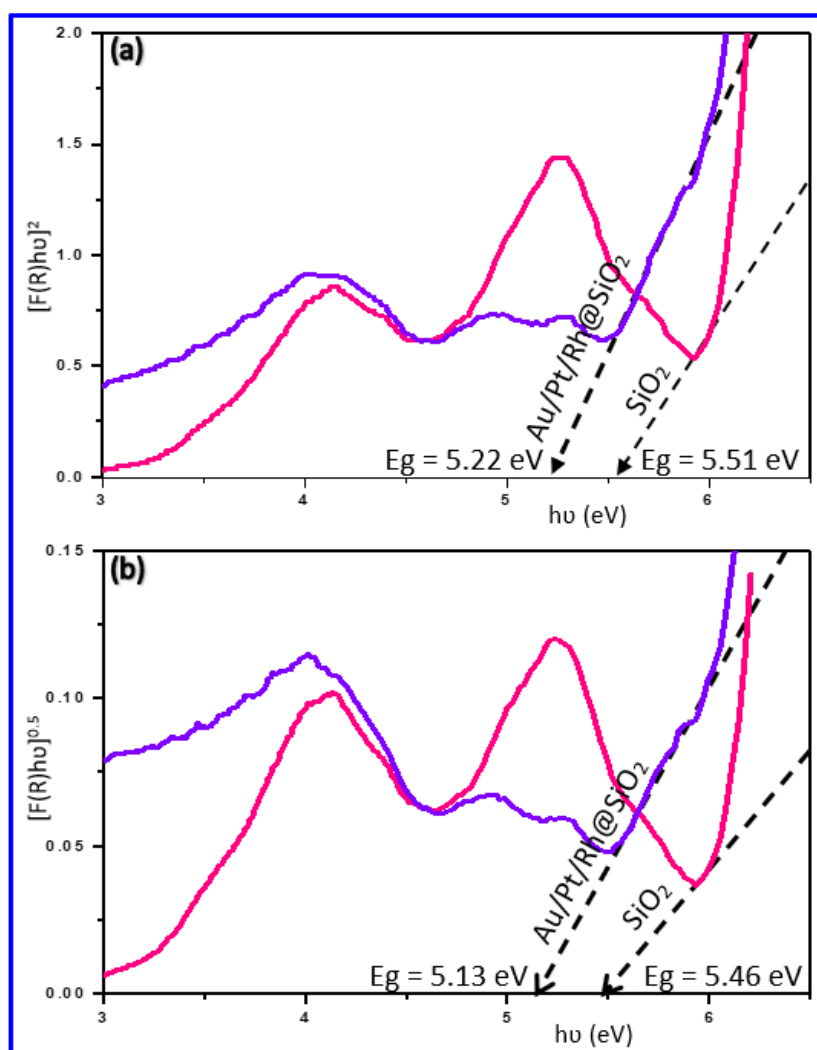

Figure 9. (**a**) Direct and (**b**) indirect band gaps of SiO$_2$ and Au/Pt/Rh@SiO$_2$ nanocomposite.

3.6. Computer simulations.

Figure 10 shows the optimized structures of SiO$_2$ and Si$_9$O$_{18}$Rh$_6$. HOMO-LUMO energy gap (Eg) values of B3LYP/Lanl2DZ optimized SiO$_2$ and Si$_9$O$_{18}$Rh$_6$ cluster are supplied in Table 2. In Au/Pt/Rh TNCs, Au/Pt bimetallic nanoparticles are surrounded by Rh particles. From the Eg values of the optimized structures, one can notice that the band gap of Si$_9$O$_{18}$Rh$_6$ is remarkably lower than that of SiO$_2$. The findings further revealed that the Au/Pt/Rh@SiO$_2$ nanocomposite would be useful as a photocatalyst. The synergism factor resulting from the interaction between the metallic core and siliceous shell might have enhanced the photocatalytic activity towards the decolorization of MV dye.
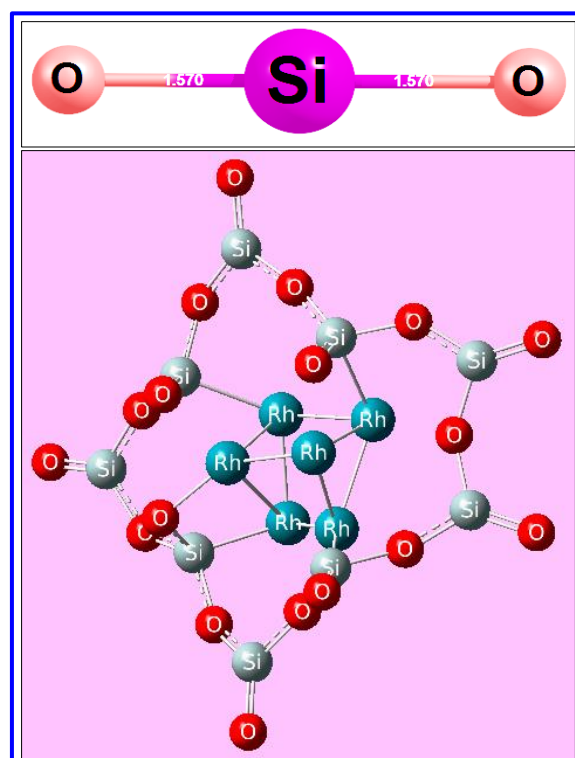
Figure 10. DFT-optimized structures of (**a**) SiO_2 and (**b**) $Si_9O_{18}Rh_6$ using a B3LYP/Lanl2DZ level of theory.
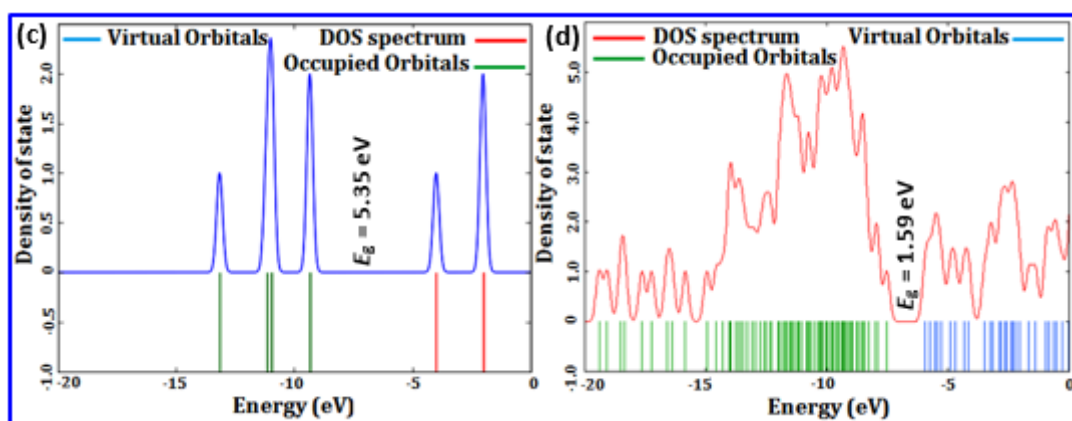
Figure 10. Electronic density of states (DOS) plot of the DFT optimized (**c**) SiO_2 and (**d**) $Si_9O_{18}Rh_6$ using a B3LYP/Lanl2DZ level of theory (***Inset***: Energy gap values in eV).

Table 2. B3LYP/Lanl2DZ optimized SiO_2 and $Si_9O_{18}Rh_6$ cluster and *HOMO-LUMO* energy gap (E_g) values.

Optimized structures	E_{LUMO} (in eV)	E_{HOMO} (in eV)	E_g (in eV)
SiO_2	-3.99	-9.34	5.35
$Si_9O_{18}Rh_6$	-5.93	-7.54	1.59

3.7. Photocatalytic activity.

Figure 11 illustrates the catalytic activity of Au/Pt/Rh@SiO_2 nanocomposites in the decolorization of MV from aqueous solution at different irradiation times under UV-A light irradiation. The photocatalytic reaction monitored by reading the absorbance of the test solution over time shows a gradual decline in the intensity along with a hypsochromic shift, confirming the effective decolorization of the MV dye. Figure 12 portrays the comparative photocatalytic activity of bare SiO_2 nanocomposite and Au/Pt/Rh@SiO_2. From Fig. 12(a-c), it can be confirmed that the Au/Pt/Rh@SiO_2 nanocomposite acts as an efficient catalyst, the precursors

used to fabricate it. The Au/Pt/Rh@SiO$_2$ nanocomposite decolorized the MV aqueous solution to 99.7 %, confirming its catalytic activity.
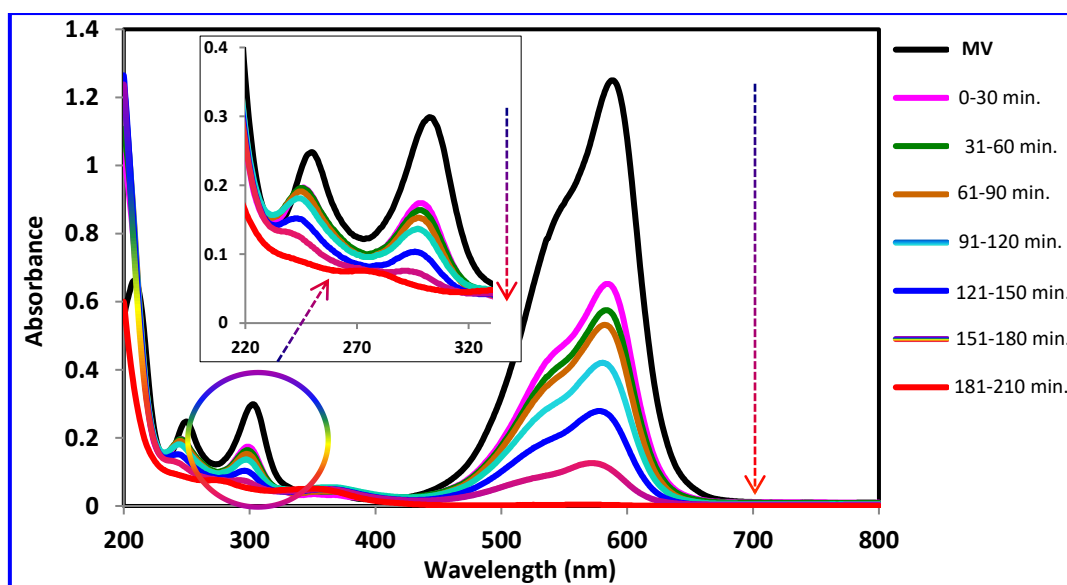

Figure 11. The changes in UV-vis spectra of MV (0.2 X 10^{-4} M) on irradiation with UV-A light in the presence of Au/Pt/Rh@SiO$_2$ nanocomposite; catalyst suspended 2.5 g/L; (***i***) MV, (***ii***) 1-30, (***iii***) 31-60, (***iv***) 61-90, (***v***) 91-120, (***vi***) 121-150, (***vii***) 151-180, (***viii***) 181-210 min, respectively.
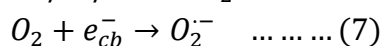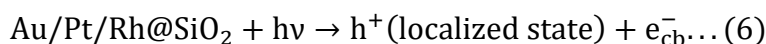
3.7.1. Reusability.

In order to examine the reusability of the photocatalysts, they were tested after use to see the stability of their photocatalytic activity. It was observed that the photocatalyst could be used for the fourth time with nearly 97% efficiency. After use, the photocatalysts were separated from the solution by centrifugation, washed three times with an ethanol-acetone solution, and then dried in an oven at 80°C overnight. The results obtained show that the decolorization of MV (%) as 99.7, 98.5, 97.9, and 97.0 for Cycle I – IV, respectively, by the photocatalyst, have been confirmed, and the data is compiled in Table 3.
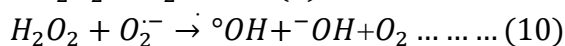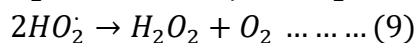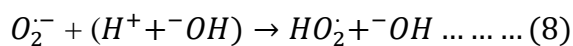
Table 3. Reusability of SiO$_2$ nanopowder, Au/Pt/Rh trimetallic colloidal nanocomposite, and Au/Pt/Rh@SiO$_2$ nanocomposite for decolorizing an aqueous solution of MV dye.

Reusability (%)	SiO$_2$ nanopowder	Au/Pt/Rh trimetallic colloidal nanocomposite	Au/Pt/Rh@SiO$_2$ nanocomposite
Cycle - I	47.2	66.5	99.7
Cycle - II	46.3	64.2	98.5
Cycle - III	44.8	62.1	97.9
Cycle - IV	42.0	58.7	97.0

3.7.2. Mechanism discussion.

For obtaining a high-performance photocatalyst, the following two essential factors are considered, (i) high-surface area [37, 38] and (ii) nano-size-based materials. Moreover, the adsorption of the dye molecules onto the catalyst surface facilitated by the photoactive sites is a key step [10, 19, 39-41]. The following steps (Eqns. 6-10) have been proposed for the entire catalytic reaction.

$$Au/Pt/Rh@SiO_2 + h\nu \rightarrow h^+(\text{localized state}) + e_{cb}^- \dots (6)$$
$$O_2 + e_{cb}^- \rightarrow O_2^{\cdot-} \quad \dots \dots \dots (7)$$

$$O_2^{\cdot-} + (H^+ + {}^-OH) \rightarrow HO_2^{\cdot} + {}^-OH \ldots \ldots \ldots (8)$$

$$2HO_2^{\cdot} \rightarrow H_2O_2 + O_2 \ldots \ldots \ldots (9)$$

$$H_2O_2 + O_2^{\cdot-} \rightarrow {}^{\cdot}\,{}^{\circ}OH + {}^-OH + O_2 \ldots \ldots \ldots (10)$$
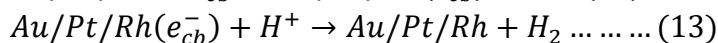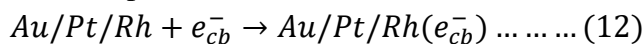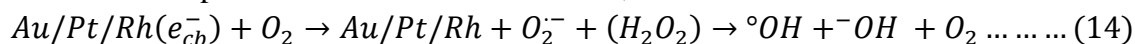
h^+ interacts with H^+ and ^-OH to form ${}^{\bullet}OH$, which attacks the MV dye molecules [10].

$$H_2O + h^+ (\text{localized state}) \rightarrow {}^{\circ}OH + H^+ \ldots \ldots \ldots (11)$$
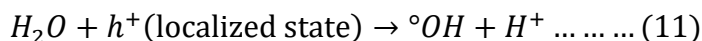
Equations 12-14 clarify the process involved in multimetallic core of SiO_2 nanocomposites.

$$Au/Pt/Rh + e_{cb}^- \rightarrow Au/Pt/Rh(e_{cb}^-) \ldots \ldots \ldots (12)$$

$$Au/Pt/Rh(e_{cb}^-) + H^+ \rightarrow Au/Pt/Rh + H_2 \ldots \ldots \ldots (13)$$

This step favoured the formation of ${}^{\bullet}OH$,

$$Au/Pt/Rh(e_{cb}^-) + O_2 \rightarrow Au/Pt/Rh + O_2^{\cdot-} + (H_2O_2) \rightarrow {}^{\circ}OH + {}^-OH + O_2 \ldots \ldots \ldots (14)$$

The MV molecule is presumably attacked by an ${}^{\bullet}OH$ radical, eliminating one or more methyl radicals. In the subsequent step, it combines with another hydroxyl radical to form a hydroxyl intermediate, which is further attacked by ${}^{\bullet}OH$.
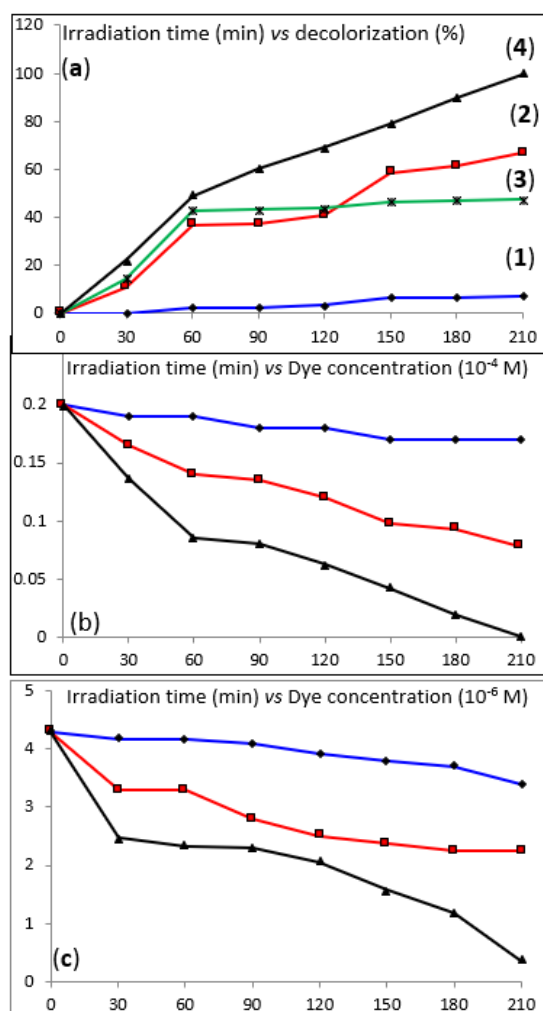
Figure 12. Comparisons of the photocatalytic activity ((**a**) UV-A light irradiation time (min) *versus* dye decolorization (%), (**b**) UV-A light irradiation time (min) *versus* concentration of the aqueous solution of MV dye (10^{-4} M) and (**c**) UV-A light irradiation time (min) *versus* concentration of the aqueous solution of MV dye (10^{-6} M)); *1*-Nil catalyst, *2*-SiO_2 nanocomposite, *3*-Au/Pt/Rh TNCs and *4*-Au/Pt/Rh@SiO_2 nanocomposite.

4. Conclusions

To conclude, a trimetallic nanocomposite, Au/Pt/Rh@SiO$_2$ has been fabricated adopting a sol-gel process, where the Au/Pt/Rh core gets encapsulated in a SiO$_2$-rich shell. HR-TEM results show that Au/Pt/Rh@SiO$_2$ nanocomposites have a finite spherical morphology with core and shell forms. Similarly, the AFM results confirm a notable variation in surface morphology and size between the bare SiO$_2$ and the doped nanocomposites. The chemical compositions of the different regions of the particles were measured by FE-SEM and EDX analysis. Au/Pt/Rh@SiO$_2$ nanocomposite was used as a photocatalyst to decolorize MV dye. The decolorization of MV by Au/Pt/Rh, TNCs, and Au/Pt/Rh@SiO$_2$ nanocomposites has also been studied by altering dye concentration, irradiation time, and catalyst dosage. Computational studies help in ascertaining the role of Au/Pt/Rh core in enhancing the photocatalytic decolorization properties of SiO$_2$ shell due to the reduction of electron–hole recombination. The overall results indicated that Au/Pt/Rh@SiO$_2$ nanocomposites could be a suitable candidate for photocatalytic application.

Funding

Acknowledgments

Conflicts of Interest

The authors declare that they have no known competing financial interests or personal relationships that could have appeared to influence the work reported in this paper.

References

1. Young Wook Lee; Hochan Ahn; Seung Eun Lee; Hyunje Woo; Sang Woo Han. Fine control over the compositional structure of trimetallic core-shell nanocrystals for enhanced electrocatalysis. *ACS Appl. Mater. Interfaces* **2019,** *11,* 25901–25908, https://doi.org/10.1021/acsami.9b06498.
2. Hao Chen; Chaoqun Guan; Hongbin Feng. Pt-based high-entropy alloy nanoparticles as bifunctional electrocatalysts for hydrogen and oxygen evolution. *ACS Appl. Nano Mater.* **2022,** *5,* 9810-9817, https://doi.org/10.1021/acsanm.2c02003.
3. Jiaheng Peng; Peng Tao; Chengyi Song; Wen Shang; Tao Deng; Jianbo Wu. Structural evolution of Pt-based oxygen reduction reaction electrocatalysts. *Chinese J. Catal.* **2022,** *43,* 47-58, https://doi.org/10.1016/S1872-2067(21)63896-2.
4. Jia Du; Jonathan Quinson; Alessandro Zana; Matthias Arenz. Elucidating Pt-based nanocomposite catalysts for the oxygen reduction reaction in rotating disk electrode and gas diffusion electrode measurements. *ACS Catal.* **2021,** *11,* 7584-7594, https://doi.org/10.1021/acscatal.1c01496.
5. Kang Wang; Li Li; Yannan Liu; Maonan Yang; Ying Wang; Xiaoyue Sun; Yanzhen Cao; Yan Yu. Enhanced photocatalytic performance and stability of multilayer core-shell nanocomposite C@Pt/MoS$_2$@CdS with full-

spectrum response. *Int. J. Hydrog. Energy.* **2022,** *47,* 12914-12926, https://doi.org/10.1016/j.ijhydene.2022.02.038.

6. Loganathan, B.; Chandraboss, V.L.; Senthilvelan, S.; Karthikeyan, B. Surface enhanced vibrational spectroscopy and first-principles study of L-cysteine adsorption on noble trimetallic Au/Pt@Rh cluster. *Phys. Chem. Chem. Phys.* **2015,** *17,* 21268-21277, https://doi.org/10.1039/C4CP05170J.

7. Xiaohong Yang; Jinnan Liang; Haitao Fu; Xiaoli Ran; Xizhong An. Fabrication of Au-Ag@TiO$_2$ ternary core-shell nanostructures with enhanced sunlight photocatalytic activity. *Powder Technol.* **2022,** *404,* 117463, https://doi.org/10.1016/j.powtec.2022.117463.

8. Shushay Hagos Gebre. Synthesis and potential applications of trimetallic nanostructures. *New. J. Chem.* **2022,** *46,* 5438-5459, https://doi.org/10.1039/D1NJ06074K.

9. Shanshan Wei; Haolin Xiao; Miao Gu; Zhencheng Chen; Liangli Cao. Ultrasensitive label-free electrochemical immunosensor based on core-shell Au@PtNPs functionalized rGO-TEPA/PB nanocomposite for HBsAg detection. *J. Electroanal. Chem.* **2021,** *890,* 115216, https://doi.org/10.1016/j.jelechem.2021.115216.

10. Jae Uk Hur; Jae Rok Shin; Jin Soon Han; Young Hwan Kim; Gye Seok An. Self-assembled core-shell Fe$_3$O$_4$-Pt nanoparticles via silylation/polymerization-based amino-functionalization. *Colloids Interface Sci. Commun.* **2022,** *50,* 100655, https://doi.org/10.1016/j.colcom.2022.100655.

11. James W. M. Crawley; Isla E. Gow; Naomi Lawes; Igor Kowalec; Lara Kabalan; C. Richard A. Catlow; Andrew J. Logsdail; Stuart H. Taylor; Nicholas F. Dummer; Graham J. Hutchings. Heterogeneous Trimetallic Nanoparticles as Catalysts. *Chem. Rev.* **2022,** *122,* 6795-6849, https://doi.org/10.1021/acs.chemrev.1c00493.

12. Xuan-Hung Pham; Van-Khue Tran; Eunil Hahm; Yoon-Hee Kim; Jaehi Kim; Wooyeon Kim; Bong-Hyun Jun. Synthesis of Gold-Platinum core-shell nanoparticles assembled on a silica template and their peroxidase nanozyme properties. *Int. J. Mol. Sci.* **2022,** *23,* 6424, https://doi.org/10.3390/ijms23126424.

13. Guohao Xu; Xuedong Zhu. A core-shell structured Zn/SiO$_2$@ZSM-5 catalyst: Preparation and enhanced catalytic properties in methane co-aromatization with propane. *Appl. Catal. B-Environ.* **2021,** *293,* 120241. https://doi.org/10.1016/j.apcatb.2021.120241.

14. Xueru Zhao; Kotaro Sasaki. Advanced Pt-based core–shell electrocatalysts for fuel cell cathodes. *Acc. Chem. Res.* **2022,** *55,* 1226-1233. https://pubs.acs.org/doi/10.1021/acs.accounts.2c00057.

15. Philipp Weber; Daniel J. Weber; Carsten Dosche; Mehtap Oezaslan. Highly durable Pt-based core–shell catalysts with metallic and oxidized Co species for boosting the oxygen reduction reaction. *ACS Catal.* **2022,** *12,* 6394-6408, https://doi.org/10.1021/acscatal.2c00514.

16. Hongjing Wang; Shiqian Jiao; Songliang Liu; Shengqi Wang; Tongqing Zhou; You Xu; Xiaonian Li; Ziqiang Wang; Liang Wang. Mesoporous bimetallic Au@Rh core–shell nanowires as efficient electrocatalysts for pH-universal hydrogen evolution. *ACS Appl. Mater. Interfaces* **2021**, *13,* 30479-30485, https://doi.org/10.1021/acsami.1c01796.

17. Kohei Aso; Hirokazu Kobayashi; Shotaro Yoshimaru; Xuan Quy Tran; Miho Yamauchi; Syo Matsumura; Yoshifumi Oshima. Singular behaviour of atomic ordering in Pt–Co nanocubes starting from core–shell configurations. *Nanoscale,* **2022,** *14,* 9842-9848, https://doi.org/10.1039/D2NR01982E.

18. Jianfeng Zhang; Ruya Cao; Wencheng Song; Lei Liu; Jiaxing Li. One-step method to prepare core-shell magnetic nanocomposite encapsulating silver nanoparticles with superior catalytic and antibacterial activity. *J. Colloid Interface Sci.* **2022,** *607,* 1730-1740, https://doi.org/10.1021/cs300507a.

19. Badr, Y.; Mahmoud, M.A. Photocatalytic degradation of methyl orange by gold silver nano-core/silica nano-shell. *J. Phys. Chem. Solids* **2007,** *68*, 413-419, https://doi.org/10.1016/j.jpcs.2006.12.009.

20. Sayan Ganguly; Subhadip Mondal; Poushali Das; Poushali Bhawal; Tushar kanti Das; Madhuparna Bose; Sumita Choudhary; Subhashis Gangopadhyay; Amit Kumar Das; Narayan Ch. Das. Natural saponin stabilized nano-catalyst as efficient dye-degradation catalyst. *Nano-Structures & Nano-Objects.* **2018,** *16*, 86-95. https://doi.org/10.1016/j.nanoso.2018.05.002.

21. Feitai Chen; Pengfei Fang; Yuanpeng Gao; Zhi Liu; Yang Liu; Yiqun Dai. Effective removal of high-chroma crystal violet over TiO$_2$-based nanosheet by adsorption-photocatalytic degradation. *Chem. Eng. J.* **2012,** *107-113,* 204-206, https://doi.org/10.1016/j.cej.2012.07.030.

22. Jimmy Mangalam; Manish Kumar; Mahima Sharma; Monika Joshi. High adsorptivity and visible light assisted photocatalytic activity of silver/reduced graphene oxide (Ag/rGO) nanocomposite for wastewater treatment. *Nano-Structures & Nano-Objects.* **2019,** *17*, 58-66, https://doi.org/10.1016/j.nanoso.2018.11.003.

23. Vaishali N. Sonkusare; Ratiram Gomaji Chaudhary; Ganesh S. Bhusari; Alok R. Rai; Harjeet D. Juneja. Microwave-mediated synthesis, photocatalytic degradation and antibacterial activity of α-Bi$_2$O$_3$

microflowers/novel γ-Bi₂O₃ microspindles. *Nano-Structures & Nano-Objects*. **2018,** *13*, 121-131. https://doi.org/10.1016/j.nanoso.2018.01.002.

24. Moondeep Chauhan; Navneet Kaur; Pratibha Bansal; Rajeev Kumar; Sesha Srinivasan; Ganga Ram Chaudhary. Proficient photocatalytic and sonocatalytic degradation of organic pollutants using CuO nanoparticles. *Journal of Nanomaterials*. **2020,** 1-15, https://doi.org/10.1155/2020/6123178.

25. Abdollah Yari; Hamzeh Adelpour Abdoli. Sol-gel derived highly selective optical sensor for sensitive determination of the mercury (II) ion in solution. *J. Hazard. Mater.* **2010,** *178*, 713-717, https://doi.org/10.1016/j.jhazmat.2010.01.146.

26. Yuan-Hsiang Lee; Sheng Dai; Jack P. Young. Silver-doped sol–gel films as the substrate for surface-enhanced Raman scattering. *J. Raman Spect.* **1997,** *28*, 635-639, https://doi.org/10.1002/(SICI)1097-4555(199708)28:8%3C635::AID-JRS152%3E3.0.CO;2-0.

27. Klein, L.C. Sol-Gel technology for thin films, fibers, performs electronics and specialty shapes, **1988** *Noyes Publications*; Park Ridge, https://doi.org/10.1002/adma.19890010816.

28. Jeffrey Brinker C.; Carol S. Ashley; Richard A. Cairncross; Ken S. Chen; Alan J. Hurd; Scoot T. Reed; Joshua Samuel; Randall Shunk P.; Robert W. Schwartz; Cathy S. Scotto. Sol-gel derived ceramic films - fundamentals and applications. *Metallurgical and Ceramic Protective Coatings. Springer, Dordrecht.* **1996,** 112-151, https://doi.org/10.1007/978-94-009-1501-5_6.

29. Frisch, M.J.; Trucks, G,W.; Schlegel, H.B.; Scuseria, G.E.; Robb, M.A.; Cheeseman, J,R.; Zakrzewski, V.G.; Montgomery Jr J.A.; Stratmann, R.E.; Burant, J.C., Dapprich, S.; Millam, J.M.; Daniels, A.D.; Kudin, K.N.; Strain, M.C.; Farkas, O.; Tomasi, J.; Barone, V.; Cossi, M.; Cammi, R.; Mennucci, B.; Pomelli, C.; Adamo, C.; Clifford, S.; Ochterski, J.; Petersson, G.A.; Ayala, P.Y.; Cui, Q.; Morokuma, K.; Malick, D.M.; Rabuck, A.D.; Raghavachari, K.; Foresman, J.B.; Cioslowski, J.; Ortiz, J.V.; Stefanov, B.B.; Liu, G.; Liashenko, A.; Piskorz, P.; Komaromi, I.; Gomperts, R.; Martin, R.L.; Fox, D.J.; Keith, T.; Al-Laham, M.A.; Peng, C.Y.; Nanayakkara, A.; Gonzalez, C.; Challacombe, M.; Gill, P.M.W.; Johnson, B.; Chen, W.; Wong, M.W.; Andres, J.L.; Gonzalez, C.; Head-Gordon, M.; Replogle, E.S.; Pople, J.A. Gaussian 03, Revision B.05, Gaussian Inc., Pittsburgh, PA, 2003.

30. Becke, A.D. Density functional thermochemistry. III. The role of exact exchange, *J. Chem. Phys.* **1993,** *98*, 5648-5652, https://doi.org/10.1063/1.464913.

31. Lee, C.; Yang, W.; Parr, R.G. Development of the colle-salvetti correlation-energy formula into a functional of the electron density. *Phys. Rev. B Condens. Matter.* **1988,** *37*, 785-789, https://doi.org/10.1103/PhysRevB.37.785.

32. Dunning Jr, T.H.; Hay, P.J. In modern theoretical chemistry, ed. H.F. *Schaefer III* **1976**, *3*, 1-28.

33. Qizhao Wang; Guoxia Yun; Ning An; Yanbiao Shi; Jiafeng Fan; Haohao Huang; Bitao Su. The enhanced photocatalytic activity of Zn²⁺ doped TiO₂ for hydrogen generation under artificial sunlight irradiation prepared by sol-gel method. *J. Sol-Gel. Sci. Technol.* **2015,** *73*, 341-349, https://doi.org/10.1007/s10971-014-3538-7.

34. Sing, K.S.W.; Everett, D.H.; Haul, R.A.W.; Moscou, L.; Pierotti, R.A.; Rouquerol, J.; Siemieniewska, T. Reporting physisorption data for gas/solid systems with special reference to the determination of surface area and porosity. *Pure Appl. Chem.* **1985,** *57*, 603-619, https://doi.org/10.1515/iupac.57.0007.

35. Rouquerol, F.; Rouquerol, J.; Sing, K. Adsorption by powders and porous solid: Principle, methodology, and applications. (1999) Academic Press, San Diego, https://www.sciencedirect.com/book/9780125989206/adsorption-by-powders-and-porous-solids.

36. Sreethawong, T.; Ngamsinlapasathian, S.; Yoshikawa, S. Surfactant-aided sol-gel synthesis of mesoporous-assembledTiO₂-NiO mixed oxide nanocrystals and their photocatalytic azo dye degradation activity. *Chem. Engg. J.* **2012,** *192*, 292-300, https://doi.org/10.1016/j.cej.2012.04.006.

37. Zhang, S.; Li, J.; Zeng, M.; Li, J.; Xu, J.; Wang, X. Bandgap engineering and mechanism study of nonmetal and metal ion codoped carbon nitride: C+Fe as an example. *Chem. Eur. J.* **2014,** *20*, 9805-9812, https://doi.org/10.1002/chem.201400060.

38. Wei, W.; Yu, C.; Zhao, Q.F.; Li, G.S.; Wan, Y. Improvement of the visible-light photocatalytic performance of TiO₂ by carbon mesostructures. *Chem. Eur. J.* **2013,** *19*, 565-576, https://doi.org/10.1002/chem.201202691.

39. Chandraboss, V.L.; Senthilvelan, S.; Natanapatham, L.; Murugavelu, M.; Loganathan, B.; Karthikeyan, B. Photocatalytic effect of Ag and Ag/Pt doped silicate non crystalline material on methyl violet-experimental and theoretical studies. *J. Non-Cryst. Solids* **2013,** *368*, 23-28, http://dx.doi.org/10.1016/j.jnoncrysol.2013.02.027.

40. Yoshida, H.; Murata, C.; Hattori, T. Screening study of silicasupported catalysts for photoepoxidation of propene by molecular oxygen. *J. Catal.* **2000,** *194*, 364-372. https://doi.org/10.1006/jcat.2000.2952.

41. Skuja, L. Time-resolved low temperature luminescence of non-bridging oxygen hole centers in silica glass. *Solid State Commun.* **1992,** *84*, 613-616, https://doi.org/10.1016/0038-1098(92)90201-J.

Supplementary Material

1. Synthesis of trimetallic Au/Pt/Rh colloidal nanocomposites

PVP-protected metal particles were synthesized according to the reported method [6]. Briefly, 0.02 g of rhodium trichloride trihydrate and 0.7 g of poly (vinyl pyrrolidone) were separately dissolved in 100 mL of distilled ethanol. 50 mL of each were pipetted out into a round bottom flask and refluxed for 5 hrs. Color change of the solution to dark brown indicated the formation of rhodium nanoparticles (Rh NPs).

Trisodium citrate-reduced Au nanoparticles (Au NPs) were separately synthesized. Briefly, 0.1% gold(III) chloride trihydrate (20 mL) was heated to boil, and 1% trisodium citrate (4 mL) was then added with stirring. The reaction mixture was heated for 80 sec and cooled down to room temperature. The color change indicated the formation of Au NPs. Then, 0.1% chloroplatinic acid hydrate (20 mL) was added to the as-synthesized Au NPs followed by adding 1% trisodium citrate (4 mL) with stirring.
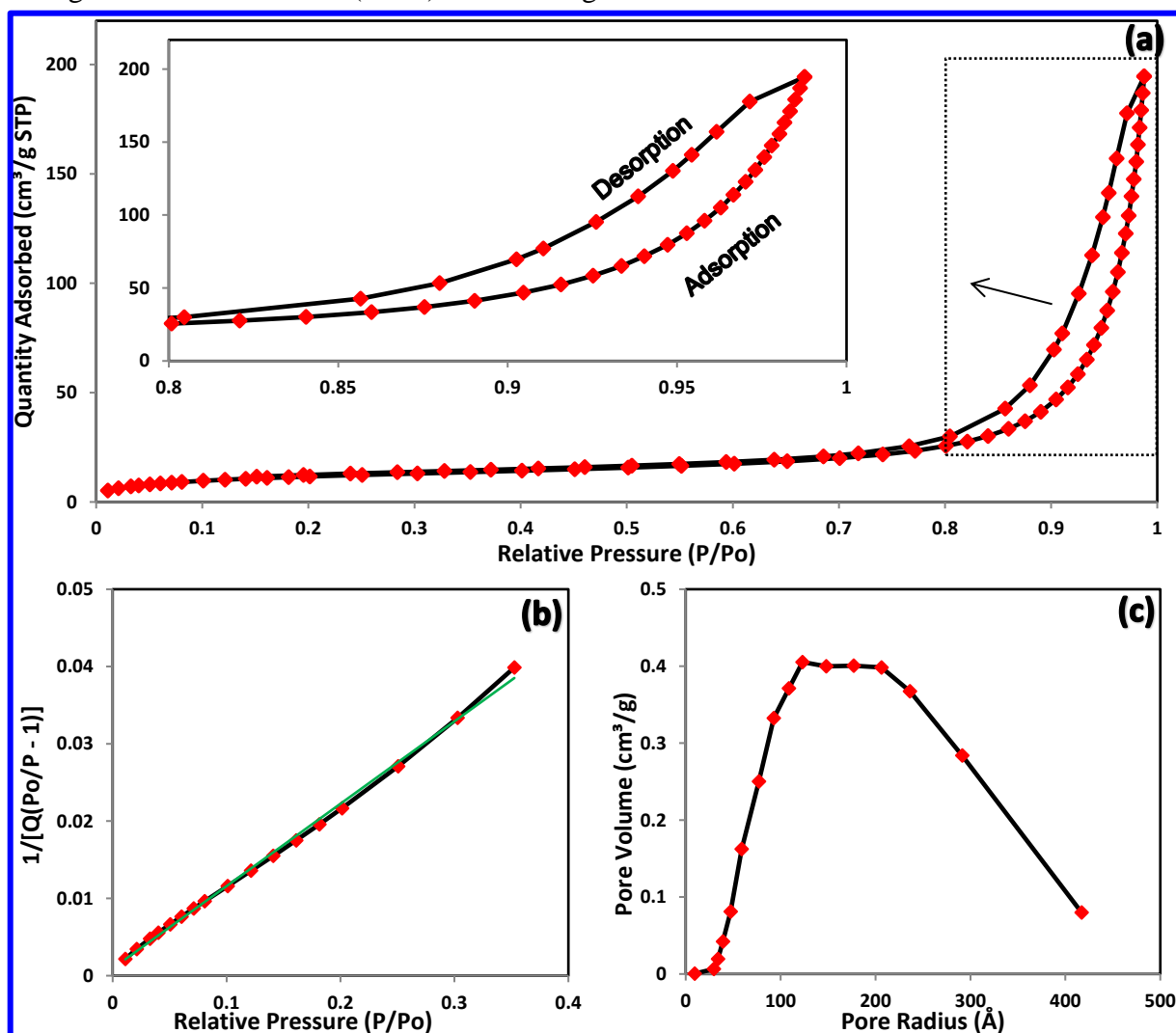

Figure S1. (a) Isotherm linear plot (nitrogen adsorption-desorption isotherms); **(b)** Brunauer-Emmett-Teller (BET) surface area plot; **(c)** Barrett-Joyner-Halenda (BJH) desorption pore volume of SiO_2 nanopowder.

The colloidal dispersions of bimetallic Au/Pt colloidal nanoparticles and mono-metallic PVP-protected Rh colloidal nanoparticles were mixed at room temperature in 1:1 ratio. The mixed dispersions were kept in stirring for a day at room temperature to complete the formation of Au/Pt/Rh TNCs.

2. Synthesis of amine-functionalized silica nanocomposite (SiO₂ nanocomposite)

TEOS (6 mL) and APTES (2 mL) were added to distilled ethanol (6 mL). This resulting mixture was poured into a shielded beaker to avoid evaporation. The mixture was stirred for 30 min at room temperature to obtain a fine formation of sol-gel material. This product was placed in a hot-air oven for 12 h at 100 °C for the complete hydrolysis of TEOS/APTES to form SiO_2 nanocomposite. The obtained zero-gel matrix was ground well to obtain a final form of SiO_2 nanocomposite.